Nucleic Acids Research, 2025, **53**, gkaf123
https://doi.org/10.1093/nar/gkaf123
Genome integrity, repair and replication

Mug20–Rec25–Rec27 binds DNA and enhances meiotic DNA break formation via phase-separated condensates

Max F. Wang [1,2,†], Meng-Yun Li [1,†], Ya-Ching Yang [1], Yu-Chien Chuang [3], Chieh-Yu Tsai [4], Mai-Chi Nguyen Binder [3], Lijuan Ma [3,5], Sheng-Wei Lin [6], Hung-Wen Li [4], Gerald R. Smith [3], Peter Chi [1,6,*]

[1]Institute of Biochemical Sciences, National Taiwan University, Taipei 10617, Taiwan
[2]Present address: Division of Chemistry and Chemical Engineering, California Institute of Technology, Pasadena, CA 91125, United States
[3]Division of Basic Sciences, Fred Hutchinson Cancer Center, Seattle, WA 98109, United States
[4]Department of Chemistry, National Taiwan University, Taipei 10617, Taiwan
[5]Present address: Dr. Neher's Biophysics Laboratory for Innovative Drug Discovery, State Key Laboratory of Quality Research in Chinese Medicine, Macau University of Science and Technology, Macau, 999078, China
[6]Institute of Biological Chemistry, Academia Sinica, Taipei 11529, Taiwan

[*]To whom correspondence should be addressed. Email: peterhchi@ntu.edu.tw
[†]The first two authors should be regarded as Joint First Authors.

Abstract

During meiosis, programmed DNA double-strand breaks (DSBs) are formed at hotspots to initiate homologous recombination, which is vital for reassorting genetic material. In fission yeast, the linear element (LinE) proteins Mug20, Rec25, and Rec27 interdependently bind chromosomal hotspots with high specificity and are necessary for high-level DSB formation. However, their mechanistic role in regulating the meiotic DSB machinery remains unknown. Here, using purified Mug20–Rec25–Rec27 (MRR) complex and functional intracellular analyses, we reveal that the MRR–DNA nucleoprotein complex assembles phase-separated condensates that compact the DNA. Notably, MRR complex formation is a prerequisite for DNA binding and condensate assembly, with Rec27 playing a pivotal role in directly binding DNA. Consistent with this finding, failure to form MRR–DNA condensates results in defective intracellular meiotic DSB formation and recombination. Our results provide mechanistic insights into how LinEs enhance meiotic DSB formation and provide a paradigm for studies in other species.

Graphical abstract

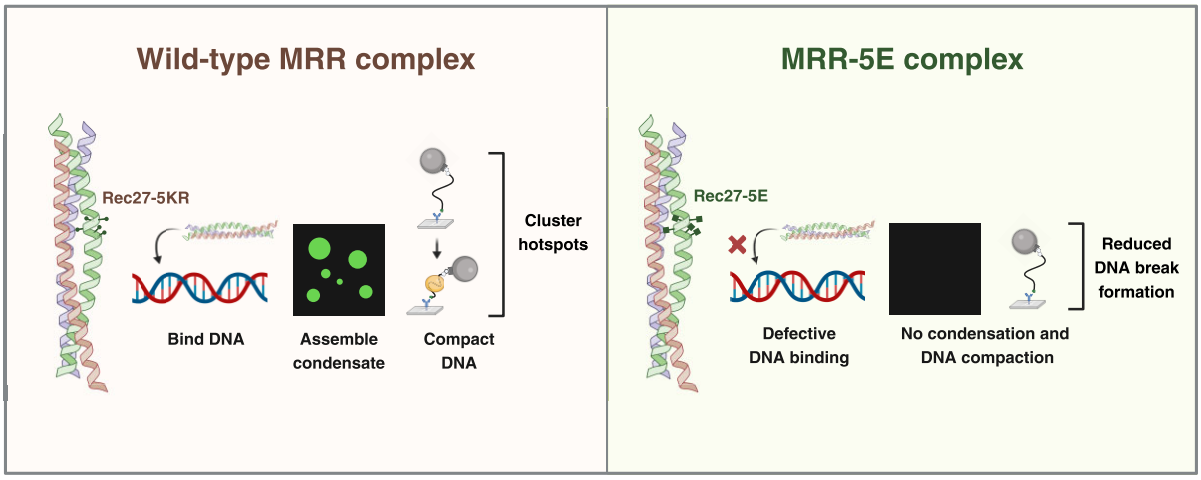

Introduction

Meiosis, a sophisticated process in all sexually reproducing species, massively influences genome evolution. During the first meiotic prophase, homologous chromosomes are stably paired and undergo meiotic recombination to reshuffle the genetic material. The reciprocal exchange of portions of homologous chromosomes generates crossovers that impart physical tension, aiding proper chromosome segregation and

Received: June 8, 2024. **Revised:** January 26, 2025. **Editorial Decision:** February 3, 2025. **Accepted:** February 7, 2025

reassorting genetic variations, thereby increasing genetic diversity [1, 2].

Meiotic recombination is initiated by programmed DNA double-strand breaks (DSBs), promoted by the conserved topoisomerase VI-like protein Spo11 [3–6]. These DSBs are not randomly or uniformly distributed across chromosomes. Instead, they are preferentially formed at specific chromosomal sites called DSB hotspots [7–11], defined as chromosomal loci that match or exceed a given threshold of Spo11-dependent DSBs in eukaryotes [9–15].

Hotspot determination among different species involves a complex interplay of multiple factors, including specific DNA sequences [16], accessible chromatin regions [10], and chromosome-bound proteins [9, 10, 17], but the mechanism has been largely elusive. For instance, hotspots are frequently located within nucleosome-depleted regions in *Saccharomyces* spp. [10, 18] and *Arabidopsis thaliana* [19, 20], but less so in the fission yeast *Schizosaccharomyces pombe* [9, 21]. In the budding yeast *S. cerevisiae* and mice, histone H3K4 methylation is correlated with DSB formation at most hotspots [22–24], whereas in *S. pombe*, the level of histone H3K9 acetylation is elevated at hotspots [25] and the histone variant H2A.Z is required for hotspot localization of DSB-forming proteins [26]. The role of these histone modifications in hotspot determination is unclear.

In *S. pombe*, linear element (LinE) proteins, which are meiosis-specific and resemble the axial element precursors of the synaptonemal complex in most eukaryotes [27, 28], bind to hotspots with high specificity and are required for high levels of DSB formation at most hotspots under reported conditions [9]. Four LinE proteins—Rec10, Mug20, Rec25, and Rec27—have been identified [27, 29, 30]. Rec10, Rec27, and Mug20 exhibit limited amino acid sequence similarity to the *S. cerevisiae* axial element protein Red1, the nematode *Caenorhabditis elegans* synaptonemal complex protein SYP-2, and its associated protein DDL-1 [8, 27, 31], respectively. However, unlike the evolutionarily conserved ultrastructure of the synaptonemal complex, which is a continuous end-to-end structure along and between homologous chromosomes, LinE proteins form shorter linear nuclear structures (LinE structures) [27]. These structures have been observed by electron microscopy upon spreading meiotic nuclei and through structured illumination fluorescence microscopy of cells at the horsetail stage (i.e., meiotic prophase I) [32–34]. Intriguingly, LinE protein structures are sensitive to 1,6-hexanediol treatment *in vivo* [34]. This aliphatic alcohol has been widely used to investigate the physical properties of self-assembling intracellular membrane-less compartments [35], typically called phase-separated condensates [36]. 1,6-hexanediol disrupts *S. pombe* LinE structures, indicating that LinE proteins undergo phase separation, as do synaptonemal complexes in other species [37] despite their differences in morphology and protein components.

Genome-wide localization of LinE proteins has demonstrated that Mug20, Rec25, and Rec27 are exclusively enriched at most DSB hotspots, with exceptionally high specificity under the reported conditions, and their protein abundances are highly correlated with DSB frequency at those hotspots [8]. In the absence of any one of these proteins, DSB frequencies at hotspots are markedly reduced [29, 38]. These proteins appear to function as a complex based on yeast two-hybrid analyses [29], their interdependencies, and the colocalization of their nuclear foci [8, 30, 34]. Notably, most meiotic DSBs are eradicated in *rec27*Δ strains [8, 39]. The genome-wide distributions of Rec27 in the absence or presence of Rec12 (the Spo11 ortholog in *S. pombe*) [5] are indistinguishable, implying that Rec27 localizes to chromosomal sites poised to be hotspots prior to DSB formation [8]. Moreover, Rec12 binds to multiple chromosomal sites but forms DSBs primarily in the company of Rec27 [8]. In addition, a recent study revealed that the chromosomal binding of Mug20, Rec25, and Rec27 is sufficient to create a DSB hotspot [40]. In that study, the authors fused one or another of these three LinE proteins with the *Escherichia coli* LacI repressor and a nuclear localization signal, localized them to a novel chromosomal site—a non-hotspot region with multiple *lacO* substitutions—and assayed DSB formation and recombinant frequencies. Interestingly, a DSB hotspot comparable to strong endogenous hotspots was generated and was dependent on the non-fused LinE proteins. These findings indicate that Mug20, Rec25, and Rec27 are highly specific hotspot-associated proteins crucial for the enhancement of *S. pombe* meiotic recombination.

Previous genetic research has demonstrated the importance of Mug20, Rec25, and Rec27 in meiotic DSB formation and has established the recombination phenotypes of various respective mutants. Nevertheless, our understanding of the mechanistic roles of these three LinE proteins in activating the meiotic DSB machinery remains primitive due to the lack of purified recombinant proteins and functional analyses. In this study, we have established a pipeline to co-express and purify to high purity tag-free Mug20, Rec25, and Rec27 as a complex, hereafter referred to as the MRR complex. Through biochemical and single-molecule analyses, we reveal the *bona fide* DNA-binding ability of the MRR complex, which assembles phase-separated condensates with duplex DNA that compact DNA substrates. By co-incubating Mug20, Rec25, and Rec27 proteins, we demonstrate that formation of the MRR complex is crucial for its DNA binding activity and condensate formation, with Rec27 playing the primary role in protein-DNA interactions. Our study reveals the biochemical and biophysical characteristics of the MRR complex, and we propose that the constituent proteins assemble on chromosome axes, spatially and numerically controlling DSB formation by altering chromosome length.

Materials and methods

DNA substrates

To prepare the substrates for the DNA binding analysis, the linear 80-mer DNA oligonucleotide (oligo), oligo 2, with its 5′ end-labeled with fluorescein amidite (FAM), and its complementary oligo 8 were synthesized and gel purified by Genomics BioSci & Tech (sequences are listed in Supplementary Table S1). The 80-bp double-stranded DNA (dsDNA) substrate was generated by annealing oligo 2 and oligo 8, resolved in a 10% TBE (90 mM Tris-boric acid, pH 8.0, 2 mM EDTA)-polyacrylamide gel and purified with a D-Tube Dialyzer (Merck Millipore). The purified DNA substrates were concentrated with a 10-kDa cutoff Amicon Ultra Centrifugal filter (Merck Millipore) and stored in TE (10 mM Tris-HCl, pH 8.0, 0.5 mM EDTA) buffer. The supercoiled pBluescript SK (-) plasmid was purified from *E. coli* using the Mini Plus Plasmid DNA Extraction System (Viogene). To generate the linear pBluescript SK (-) plasmid, the supercoiled DNA was

digested by *Eco*RI restriction enzyme and purified using the Advanced PCR Clean Up System (Viogene).

The 1,162-bp dsDNA substrate used in the single-molecule tethered particle motion (TPM) experiment was generated by polymerase chain reaction (PCR) using the plasmid pBR322 as the template. The PCR fragments were labeled during amplification using the 5′-biotin-modified primer TPM-biotin and the 5′-digoxigenin-modified primer TPM-DIG (sequences are listed in Supplementary Table S1). All PCR products were further purified using NucleoSpin Gel and PCR Clean-up kit (MACHEREY-NAGEL).

Yeast strains and genetic methods

Genotypes of the *S. pombe* strains are described in Supplementary Table S2. Media for cell growth and methods for strain construction, meiotic crosses, and random spore analysis were as described previously [41].

Construction of *rec27-283* (5E)

The mutation *rec27-283* (5E) was introduced into plasmid pLM08 by mutagenesis using the Q5 Site-Directed Mutagenesis Kit (New England BioLabs) as described [38]. Primers to introduce the 5E mutation are listed in Supplementary Table S1. The mutation was confirmed by sequencing. Subsequently, the mutated *rec27* ORF, along with flanking homologous sequences, was released from the plasmid through *Kpn*I digestion and integrated into the chromosomal *rec27* locus by transforming strain GP8513 (*rec27-257::ura4*$^+$) to 5-fluorouracil (FOA)-resistance. Primers OL3255 and OL3256 were used to confirm the integration site [38].

Preparation of expression vectors

Full-length cDNAs of *S. pombe mug20*, *rec25*, *rec27*, and the *rec27-5E* mutant variant were cloned into pET SUMO vectors (Invitrogen) with hexahistidine (His_6) and SUMO tags by In-Fusion cloning (Takara Bio) to generate N-terminally-tagged expression vectors for Mug20, Rec25, Rec27, and Rec27-5E recombinant proteins. Superfolder green fluorescent protein (sfGFP) [42] cDNA was subcloned into the His_6-SUMO-tagged vectors of Rec27 and Rec27-5E to yield expression vectors for Rec27–sfGFP and Rec27-5E–sfGFP recombinant proteins. To generate the untagged Rec25–Mug20 expression vector, the *rec25* and the *mug20* cDNAs were cloned into the pETDuet-1 expression vector (Novagen) by In-Fusion cloning. All expression vectors were sequenced to ensure the absence of unexpected mutations.

Expression and purification of recombinant proteins

The untagged, sfGFP-conjugated Mug20–Rec25–Rec27 (MRR) protein complex, the MRR-5E mutant variant, and His_6-SUMO-tagged Rec25, -Rec27, -Rec27–sfGFP, and -Mug20 recombinant proteins were expressed in *E. coli* BL21-CodonPlus(DE3)-RIL cells containing pG-Tf2 plasmid, which enables expression of the chaperonins GroES–GroEL and the Trigger factor [43]. To express the protein complex, cells were co-transformed with pETDuet-1-Rec25–Mug20 and one of the following expression vectors: pET SUMO-His_6-SUMO-Rec27, pET SUMO-His_6-SUMO-Rec27–sfGFP, pET SUMO-His_6-SUMO-Rec27-5E, or pET SUMO-His_6-SUMO-Rec27-5E–sfGFP. The co-transformed cells were plated on LB plates containing the appropriate antibiotics. A single colony was cultured in liquid LB medium at 30°C to an optical density (OD_{600}) of 0.6–0.8. Protein expression was carried out at 12°C overnight with 0.25 mM isopropyl β-D-1-thiogalactopyranoside (IPTG).

All purification steps were carried out at 4°C. To purify the MRR complex or Rec27 recombinant protein, cell pellets were resuspended in T buffer [25 mM Tris-HCl, pH 7.5, 0.5 mM EDTA, 10% glycerol, 0.01% IGEPAL CA-630 (non-ionic detergent), and 1 mM β-mercaptoethanol] supplemented with 500 mM KCl, 1 mM phenylmethylsulfonyl fluoride (PMSF), 1 mM benzamidine, and 3 μg/mL of the following protease inhibitors: aprotinin, chymostatin, leupeptin, and pepstatin A. The resuspended cells were sonicated and centrifuged at 100,000*g* for an hour. The clarified cell lysate was incubated with pre-equilibrated Ni-NTA Agarose resin (QIAGEN) for 3 hours, washed with K buffer (20 mM KH_2PO4, pH 7.4, 0.5 mM EDTA, 10% glycerol, 0.01% IGEPAL CA-630, 1 mM β-mercaptoethanol) containing 100 mM KCl and 20 mM imidazole, and eluted with K buffer containing 100 mM KCl and 200 mM imidazole. The eluate was loaded on an 8-mL Tricorn column (Cytiva) packed with CHT ceramic hydroxyapatite Type I resin (Bio-Rad Laboratories) and fractionated through a linear gradient of 0–280 mM KH_2PO_4 in K buffer. Fractions containing the proteins of interest were pooled and dialyzed overnight with a 10-kDa cutoff dialysis membrane (Repligen) to reduce the KCl concentration to 50 mM. The dialyzed sample was loaded onto a 1-mL Tricorn column packed with SOURCE 15Q resin (Cytiva) and fractionated through a linear gradient of 0–335 mM KCl in T buffer. The His_6-SUMO tag on Rec27 was cleaved by applying SUMO protease Ulp1 overnight. The tag-free recombinant protein was then loaded onto a Superdex 200 Increase 10/300 GL column (Cytiva) pre-equilibrated with T buffer containing 300 mM KCl. The purest peak fractions, as determined by sodium dodecyl sulfate-polyacrylamide gel electrophoresis (SDS-PAGE) stained with Coomassie brilliant blue, were pooled, concentrated in a 10-kDa cutoff Amicon Ultra Centrifugal filter, aliquoted, frozen with liquid nitrogen, and stored at -80°C.

To purify the His_6-SUMO-tagged Rec25 and Mug20 recombinant proteins, the protein-expressing cells were resuspended, lysed, and centrifuged as described above. The clarified cell lysate was incubated with pre-equilibrated TALON Metal Affinity Resin (Takara Bio) for 3 hours, washed with TALON buffer (25 mM Tris-HCl, pH 7.5, 10% glycerol, 0.01% IGEPAL CA-630, 1 mM β-mercaptoethanol, 10 mM ATP, and 10 mM $MgCl_2$) containing 50 mM KCl and 10 mM imidazole, and eluted with TALON buffer containing 50 mM KCl and 200 mM imidazole. The millimolar concentrations of ATP and magnesium ions in the TALON buffer act as biological hydrotropes that solubilize proteins and keep them soluble. The eluate was loaded onto a 1-mL Tricorn column packed with SOURCE 15Q resin and fractionated through a linear gradient of 0–335 mM KCl in TALON buffer. The eluate was loaded onto a 1-mL Tricorn column packed with CHT ceramic hydroxyapatite Type I resin and fractionated through a linear gradient of 0–280 mM KH_2PO_4 in K buffer, followed by loading onto a 1-mL Mono Q 5/50 GL column (Cytiva) and elution through a linear gradient of 0–335 mM KCl in T buffer. The purest peak fractions, as determined by SDS-PAGE stained with Coomassie brilliant blue, were pooled, concentrated in a 10-kDa cutoff Amicon Ultra Centrifugal filter, aliquoted, frozen with liquid nitrogen, and stored at -80°C.

Mass photometry

The sample chamber and samples for the mass photometry experiment were prepared as described previously [44]. In brief, glass coverslips were thoroughly cleaned with Milli-Q H_2O and isopropanol and then dried with a clean nitrogen stream. Before the mass photometry experiment, the protein sample was directly diluted in phosphate-buffered saline to a concentration of 2 nM and applied to the pre-assembled silicon gasket well. All measurements were performed using a TwoMP mass photometer (Refeyn Ltd, Oxford, UK), and the data were acquired and analyzed using AcquireMP and DiscoverMP software, respectively. Calibration was carried out using the bovine serum albumin (BSA) standard.

Electrophoretic mobility shift assay

The indicated concentration of protein was incubated with 80-mer single-stranded DNA (ssDNA) (oligo 2), 80-bp ds-DNA (oligo 2 and oligo 8), or supercoiled or linear 3-kb pBluescript SK (-) plasmid at a concentration of 5 nM molecules. The 10-μL binding reactions were carried out in 35 mM Tris-HCl, pH 7.5, 150 mM KCl, 1 mM DTT, and 100 ng/μL BSA at 25°C for 20 minutes. The reaction mixtures with oligonucleotides and plasmid substrates were resolved in 0.8% agarose or 10% TBE-polyacrylamide gels in TBE buffer at 4°C. Fluorescent signals were detected for the oligonucleotide substrates, and gels were imaged using an Amersham Typhoon 5 Biomolecular Imager (Cytiva) with a 488 nm laser diode and a Cy2 515–535 nm band-pass filter. Gels were stained with 1 μg/mL ethidium bromide for the plasmid substrates and imaged with a Biomolecular Imager Gel Doc XR+ system (Bio-Rad Laboratories).

In vitro condensation assay

Unless otherwise stated, the phase-separated nucleoprotein condensates were assembled according to the following procedure. First, 5 μM protein (with 10% sfGFP-conjugated protein) and 5 nM (molecules) supercoiled pBluescript SK (-) plasmid were incubated at 25°C for 30 minutes in the reaction buffer (35 mM Tris-HCl, pH 7.5, 50 mM KCl, 1 mM DTT) to reach a final 10-μL reaction volume. After 30 minutes of incubation, 3 μL of the reaction mixture was dropped onto a microscope slide and covered with a coverslip. Micrographs were captured on a Leica TCS SP5 confocal microscope with a 100×/1.4 NA oil immersion objective lens (Olympus) and analyzed with Fiji [45]. In brief, 155 μm × 155 μm (1,024 × 1,024-pixel) micrographs were thresholded using the mean intensity of the background plus three times the standard deviation. Masked foci were counted, and the areas of all masked foci were summed.

Fluorescence recovery after photobleaching

Fluorescence recovery after photobleaching was performed on a Leica TCS SP5 confocal microscope with a 100×/1.4 NA oil immersion objective lens at room temperature. Condensates were assembled under the above-described conditions and photobleached for 1 second using a 488 nm argon laser. Time-lapse images were captured at 30-second intervals for 10 min.

Single-molecule tethered particle motion experiment

The silanized glass slides, coverslips, reaction chamber, and 220-nm streptavidin-coupled polystyrene beads (Bangs Laboratories) were prepared as previously described [46]. The reaction chamber was first incubated with 8–10 ng/μL anti-digoxigenin antibody (Roche) for 30 minutes and with 2 mg/mL BSA for 30 minutes to prevent non-specific binding. Then, 20 μL of 2–4 nM 1,162-bp dsDNA substrates were immobilized on the slide through digoxigenin/anti-digoxigenin linkage, followed by washing twice with buffer to remove unbound DNA molecules before incubating with the streptavidin-coupled polystyrene beads. The DNA tethers were incubated with 1.32 μM MRR complex in 20 μL TPM buffer (35 mM Tris-HCl, pH 7.5, 1 mM DTT, 2 μg/μL BSA, and 15 mM KCl). To dissolve the condensate on the DNA tethers, TPM buffer with 8% 1,6-hexanediol was flowed into the reaction chamber. Images of the beads were captured on an Olympus IX71 inverted optical microscope with a differential interference contrast system and a 100×/1.4 NA oil immersion objective lens. Brownian motion of the beads was defined by the standard deviation of bead centroid positions every 20 frames (30 ms/frame) for a total of 500 frames and analyzed using a custom Python script.

Spin-down assay

The indicated protein concentration was incubated with 5 nM (molecules) supercoiled pBluescript SK (-) plasmid to assemble phase-separated condensates under the conditions described above. The assembled nucleoprotein condensates were centrifuged at 15,000*g* for 10 minutes, and concentrations were measured in the clarified supernatant using the Bradford assay.

Circular dichroism spectroscopy

The secondary structures of the MRR and MRR-5E complexes (4 μM) were determined by circular dichroism (CD) analysis using a Jasco J-815 spectropolarimeter under constant nitrogen flush. The far-ultraviolet CD spectra were measured at a wavelength range of 195–250 nm, with a bandwidth of 1.0 and a resolution of 0.5 nm at a scan speed of 50 nm/min. All samples were loaded in a 1-mm quartz cuvette. Proteins were diluted in a buffer containing 20 mM NaH_2PO_4 and 150 mM NaF. All CD spectra were blanked with the respective buffer, and all measurements were performed in triplicate and averaged at 25°C.

Fluorescence microscopy

Homothallic (h^{90}) cells were induced and imaged as described previously [34]. Cells from 50–100 μL of fresh overnight culture in yeast extract liquid were collected, washed three times with water, suspended in 20 μL of water, spotted on sporulation medium (MEA), and incubated at 25°C for 13–15 hours. Cells induced for meiosis were suspended in nitrogen-depleted Edinburgh minimal medium (EMM2−N) with Hoechst 33342 (5 μg/mL) to stain chromatin. Before observation, the cell suspension was spread on a poly-L-lysine-coated slide using structured illumination microscopy with a 100×/1.4 NA STED White Objective (Leica Microsystems) and VT-iSIM system (Visitech International). Image data were processed with Micro Evolution Deconvolution Software run-

ning in Fiji. Images are maximum intensity projections of sections with a step size of 0.2 μm to cover the whole cell. For cells treated with 1,6-hexanediol, cells were suspended in EMM2−N with Hoechst 33342 and 1,6-hexanediol (7.5% w/v) and observed under a microscope within 5 minutes of adding the hexanediol. Experiments using two different sources of 1,6-hexanediol (Sigma-Aldrich and Hampton Research) generated similar results.

DSB frequency analysis and quantification

The procedures for DSB quantification were as described previously [47]. Cells (*h*$^-$ *rad50S pat1-as1* haploids) were induced for meiosis at 25°C, harvested at 0, 6, and 7 hours, and embedded in agarose plugs. Cells were lysed and treated with RNase and proteinase K. The DNA was digested overnight with a restriction enzyme (*Pme*I or *Not*I), and the fragments were separated by pulsed-field gel electrophoresis and analyzed by Southern blot hybridization. Probes for hybridization are described in Young *et al.* [48] and Fowler *et al.* [49]. Signals were detected using a Typhoon Odyssey PhosphorImager system (GE Healthcare) and quantified using ImageQuant TL software (GE Healthcare).

AlphaFold2 structure prediction

The structure of the MRR complex was predicted using ColabFold batch v1.4 with the specialized AlphaFold-multimer model and MMseqs2 server for the multiple sequence alignment (MSA) [50, 51]. The default pair MSA and filter options were used to generate five models with the highest predicted local distance difference test scores. The model with the highest score was selected in this study.

Statistical analysis

All statistical tests were performed using GraphPad Prism 10 (GraphPad Software Inc.). The normality of data was confirmed by the Shapiro–Wilk test. The heterogeneity of sample variances among groups was determined by the Brown–Forsythe test. Mean values among multiple groups were compared using one-way or two-way analysis of variance (ANOVA) with Dunnett's or Šidák's post hoc test. For comparison between the two groups, the *F* test and the unpaired *t*-test were adopted to confirm the variance heterogeneity and the statistical difference between the mean values of the two groups. $p < 0.05$ were considered to be statistically significant. All statistical tests and *p*-values are two-tailed. No statistical methods were used to predetermine the sample size.

Results

Expression and purification of *S. pombe* Mug20–Rec25–Rec27 complex

To characterize the biochemical properties of Mug20, Rec25, and Rec27 and unravel the molecular basis of their function as a complex, we sought to co-express and purify untagged Mug20, Rec25, and Rec27. To enhance the solubility of expressed proteins, hexahistidine (His_6) and SUMO tags were introduced at the N-terminus of Rec27 (Fig. 1A) and, after purification, they were removed using the SUMO protease Ulp1. Co-expressed Mug20, Rec25, and Rec27 proteins in *Escherichia coli* were verified by Coomassie brilliant blue-stained SDS-PAGE and immunoblotting (Fig. 1B), and then purified according to a multi-step purification protocol that entailed affinity, ion exchange, and size exclusion chromatography (Supplementary Fig. S1A). During each purification step, Mug20, Rec25, and Rec27 eluted in identical fractions, indicating that the MRR protein complex remained intact. The highly purified untagged MRR complex was obtained without soluble aggregates through size exclusion chromatography (Fig. 1C and Supplementary Fig. S1B), and its stoichiometry was analyzed by mass photometry. Complex size, as determined by mass photometry, matches the expectation of a monomer (49 kDa), indicating that the purified MRR complex assembles into a 1:1:1 stoichiometry (Supplementary Fig. S1C). Mug20, Rec25, and Rec27 protein identities were confirmed by liquid chromatography coupled with tandem mass spectrometry (LC–MS/MS) (Fig. 1D).

The MRR complex is a *bona fide* DNA-binding protein complex

The constituents of the MRR complex have been shown previously to colocalize at DSB hotspots and to form, interdependently, chromatin-associated LinE structures [8, 27, 29, 30]. To investigate if the intact purified MRR complex possesses DNA-binding activity, we performed an electrophoretic mobility shift assay. Using negatively supercoiled and linear dsDNA as substrates (~3 kilobases, kb), we found that the MRR complex bound both types of DNA without any significant binding preference (Fig. 2A–C). Next, we compared the binding affinity of the MRR complex for 80-base pair (bp) ssDNA and dsDNA. The protein complex bound the ssDNA and exhibited a similar DNA-binding affinity for dsDNA (Supplementary Fig. S1D, comparing panels i and ii). To further test a binding preference, both DNA substrates were co-incubated with the MRR complex in a mobility shift assay. Our results revealed a marginal preference for dsDNA binding (Fig. 2D). Taken together, these findings demonstrate that the MRR complex is a *bona fide* DNA-binding protein complex, with a slight binding preference for dsDNA, with or without ends.

DNA-driven MRR condensate assembly *in vitro*

Due to their similar amino acid sequences and morphology, LinE proteins are believed to be evolutionarily related to the ubiquitous synaptonemal complexes [27, 28]. These complexes form phase-separated structures in meiosis in the species examined to date [37]. Biomolecular phase separation is driven by cumulative electrostatic and hydrophobic interactions between intrinsically disordered regions with low amino acid sequence complexity or multivalent interactions such as protein-protein or protein-DNA interactions [52–54]. The phase-separated condensates share similar biophysical properties: they can fuse, are promoted by molecular crowding [55], and are reversible.

In vivo, nuclear foci of *S. pombe* Mug20, Rec25, and Rec27 are dissolved by 1,6-hexanediol treatment [34], indicating that they form phase-separated condensates just like the synaptonemal complexes of other species. Additionally, the FuzDrop algorithm predicts that Rec25 and Rec27 harbor disordered regions important for condensate formation (Fig. 3A) [56]. To further explore if the MRR–DNA nucleoprotein complex assembles and behaves like typical phase-separated condensates *in vitro*, we purified and visualized the MRR com-

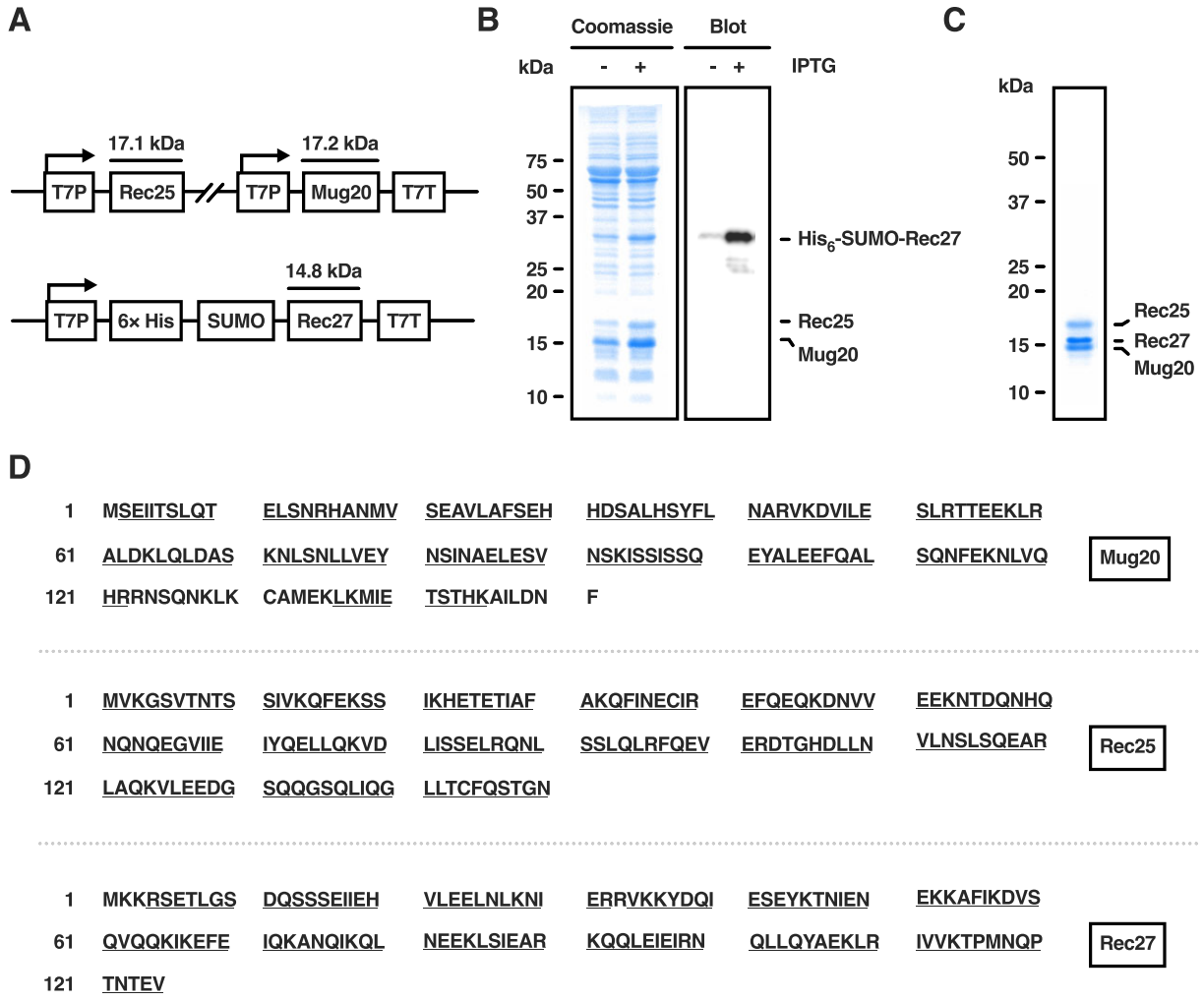

Figure 1. Expression and purification of *S. pombe* MRR complex. (**A**) Plasmid maps of Rec25, Mug20, and His_6-SUMO-tagged Rec27. T7P and T7T represent the T7 promoter and terminator, respectively. (**B**) Coomassie brilliant blue-stained SDS-PAGE and immunoblotting (hexahistidine-tag monoclonal antibody) of the whole cell extracts harboring the His_6-SUMO-Rec27 and Rec25–Mug20 expression vectors incubated with or without IPTG. The hexahistidine tag monoclonal antibody was used in the immunoblotting analysis. (**C**) SDS-PAGE of the purified untagged MRR complex (3 μg was loaded). (**D**) The identities of Mug20, Rec25, and Rec27 were determined by LC–MS/MS. The amino acids identified in the fragments are underlined.

plex conjugated to the sfGFP (Supplementary Fig. S2A and B) in the presence of supercoiled plasmid DNA. We observed that micron-sized quasi-circular condensates became visible and apparent at a protein concentration of 5 μM (Fig. 3B). These condensates grew in size and decreased in number in a concentration-dependent manner (Supplementary Fig. S3A and B). A time-course analysis revealed that the condensates appeared within 5 minutes of mixing and reached a plateau in size and number after 30 minutes, with size increasing and number decreasing over time, indicative of condensate coalescence (Fig. 3C). Additionally, condensate formed at high protein and low salt concentrations but was suppressed at high salt concentrations (Fig. 3D). No significant fluorescence recovery was observed after photobleaching (Supplementary Fig. S4A), suggesting high viscosity within a condensate [57]. Moreover, the crowding agent polyethylene glycol (PEG) strongly enhanced condensate formation (Supplementary Fig. S4B).

In addition, we determined an estimated saturation concentration (c_{sat}) using an absorbance-based spin-down assay. Above a threshold concentration (~10 μM), the concentration in the supernatant reached a plateau (Fig. 3E). This outcome is consistent with establishing phase equilibrium between the dilute and dense phases. To confirm the robustness of our assay results, we also included BSA as a negative control. The assembled condensates were dissolved upon exposure to high salt levels or 1,6-hexanediol, supporting that condensate assembly relied on electrostatic and hydrophobic interactions (Fig. 3F). In conclusion, the phase of the MRR–DNA nucleoprotein complex is not an irreversible aggregate but a stable, gel-like phase.

Surprisingly, in the absence of duplex DNA, the quasi-circular condensates still assembled but at a higher protein concentration than with DNA (Supplementary Fig. S3A and B). The biophysical characteristics of these MRR condensates are identical to those of the MRR–DNA nucleoprotein condensates, i.e., they coalesce, display high viscosity, and are reversible (Supplementary Fig. S3C–E). Hence, the MRR complex can intrinsically assemble phase-separated condensates, with duplex DNA molecules potentially acting as scaffolds for protein loading and accumulation, thereby simplifying the condensate assembly process.

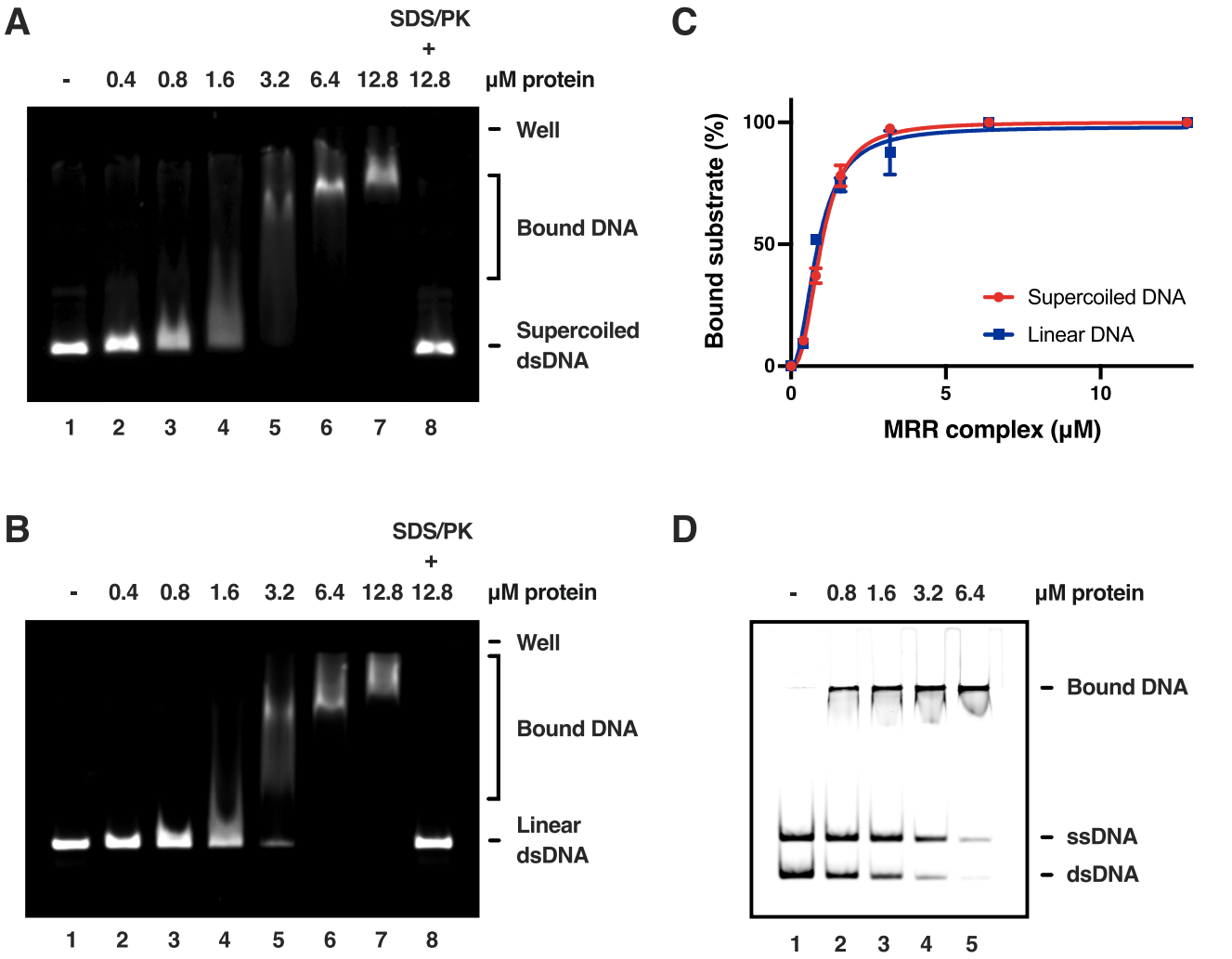

Figure 2. DNA binding properties of the MRR complex. (**A**–**B**) The indicated concentration of MRR complex was incubated with (**A**) supercoiled or (**B**) linear plasmid DNA substrates (~3 kb). The reaction mixture in lane eight was treated with SDS and proteinase K (PK) to deproteinize the nucleoprotein complex as a control. (**C**) Quantification of the gel mobility shift assay with supercoiled and linear plasmid DNA substrates. Data are shown as mean ± SD from at least two independent experiments and fitted to the Hill equation. The fitted dissociation constants (K_d) are 0.98 μM (supercoiled) and 0.86 μM (linear) with coefficients of determination (R^2) of 0.997 and 0.982, respectively. (**D**) The indicated concentration of MRR complex was co-incubated with a mixture of the 80-bp dsDNA and its constituent ssDNA. DNA was used at a concentration of 5 nM molecules.

MRR condensates compact duplex DNA

To prevent an overabundance of breaks during meiotic recombination, introduction of a DSB hotspot reduces DSB activity at neighboring hotspots [49, 58, 59]. Fowler *et al.* [49] proposed that the hotspot-amplifying LinE proteins physically cluster hotspots over a limited chromosomal interval (~200 kb or ~35 cM), leading to this phenomenon, termed "hotspot competition." This clustering behavior may be driven by condensate-mediated DNA compaction, as observed for a transcription factor that brings distant DNA regions into proximity [60]. Accordingly, we used a single-molecule TPM technique to test if the MRR–DNA nucleoprotein condensate can reduce the end-to-end distance of duplex DNA molecules. Our TPM experiment measured the Brownian motion (BM) of bead-labeled DNA molecules anchored on a glass slide (Fig. 4A), enabling real-time observation of DNA end-to-end distance alteration [61]. Compared to the DNA-only control group, the presence of the MRR complex dramatically reduced BM values of DNA-tethered beads (Fig. 4B and C), indicating that MRR–DNA condensates are more compact, with a shorter DNA end-to-end distance than the substrate DNA [62]. To confirm if the MRR condensate drove this behavior, we treated the compacted DNA molecules with 1,6-hexanediol. This treatment resulted in BM values recovering to a level determined for the DNA-only group (Fig. 4B and C), suggesting a condensate-driven DNA compaction.

Five basic amino acid residues in Rec27 account for the DNA binding activity and condensate assembly of the MRR complex

To further delve into the importance of DNA binding activity and condensate assembly in meiotic DSB formation, we sought to identify mutant variants of the MRR complex defective in either of these two characteristics. Fowler *et al.* [8] previously demonstrated that Rec27 binds to sites poised to be DSB hotspots, and most Rec12-bound sites do not form high-level breaks in the absence of Rec27, implying that Rec27 plays a crucial role in enhancing meiotic DSB formation. Furthermore, Ma *et al.* [38] identified three *rec27* missense

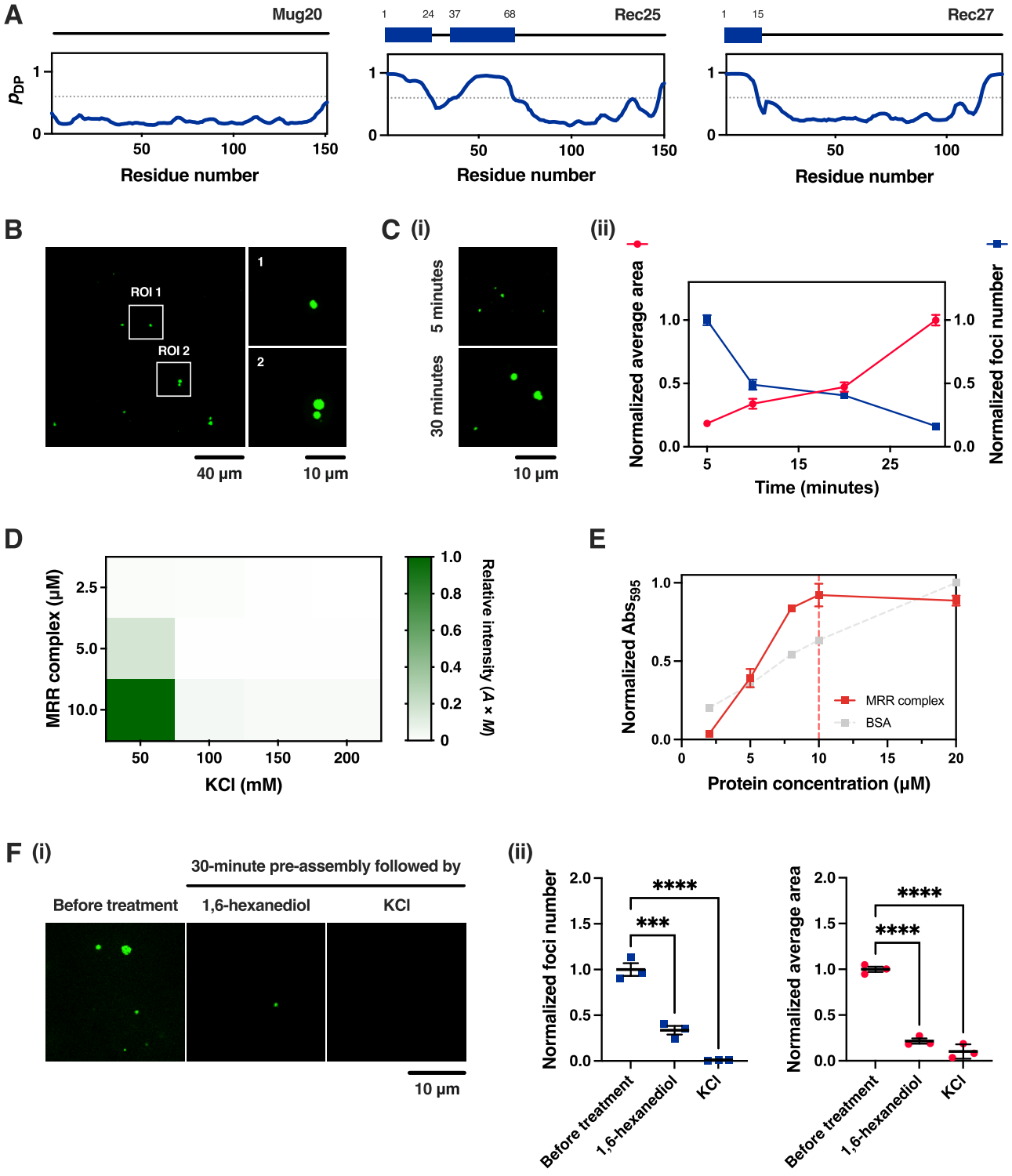

Figure 3. DNA-driven MRR condensate assembly *in vitro*. (**A**) Prediction of Mug20, Rec25, and Rec27 droplet-promoting regions using the FuzDrop server [56]. The amino acid position is shown in the *x*-axis, and the *y*-axis indicates the droplet-promoting probability (p_{DP}), where $p_{DP} = 0.6$ (dotted line) is a cutoff value above which residues are considered capable of promoting phase separation. The bars indicate the predicted droplet-promoting regions. (**B**) Representative micrograph of 5 μM MRR–DNA nucleoprotein condensates. The boxes indicate two zoomed-in regions of interest, expanded on the right. (**C**) (i) Representative micrograph of 5 μM MRR–DNA nucleoprotein condensates assembled after 5 and 30 minutes. (ii) Normalized foci number and average foci area at different time points. Numbers and average foci area were normalized to the mean of the sample assembled after 5 and 30 minutes, respectively. Data are shown as mean ± SEM from three independent experiments. (**D**) The impact of KCl and protein concentrations on MRR–DNA nucleoprotein condensate formation. The relative fluorescence intensity of condensation is represented as the average foci area multiplied by mean fluorescence intensity ($A \times M$). (**E**) The normalized absorbance at 595 nm of the clarified supernatant of the MRR complex. The vertical dashed line intersects the abscissa at ~10 μM, the inferred saturation concentration (c_{sat}) for the MRR–DNA nucleoprotein condensates. BSA was included as a control, as shown by the gray dashed line. (**F**) (i) Representative micrographs of pre-assembled MRR–DNA nucleoprotein condensates challenged with 8.3% 1,6-hexanediol or 1 M KCl. Condensates were assembled for 30 minutes before being challenged. (ii) Quantification data were normalized to the mean of the control group. Data are shown as mean ± SEM from three independent experiments. Statistical significance was determined using one-way ANOVA with Dunnett's post hoc test. ***$p < 0.001$, ****$p < 0.0001$.

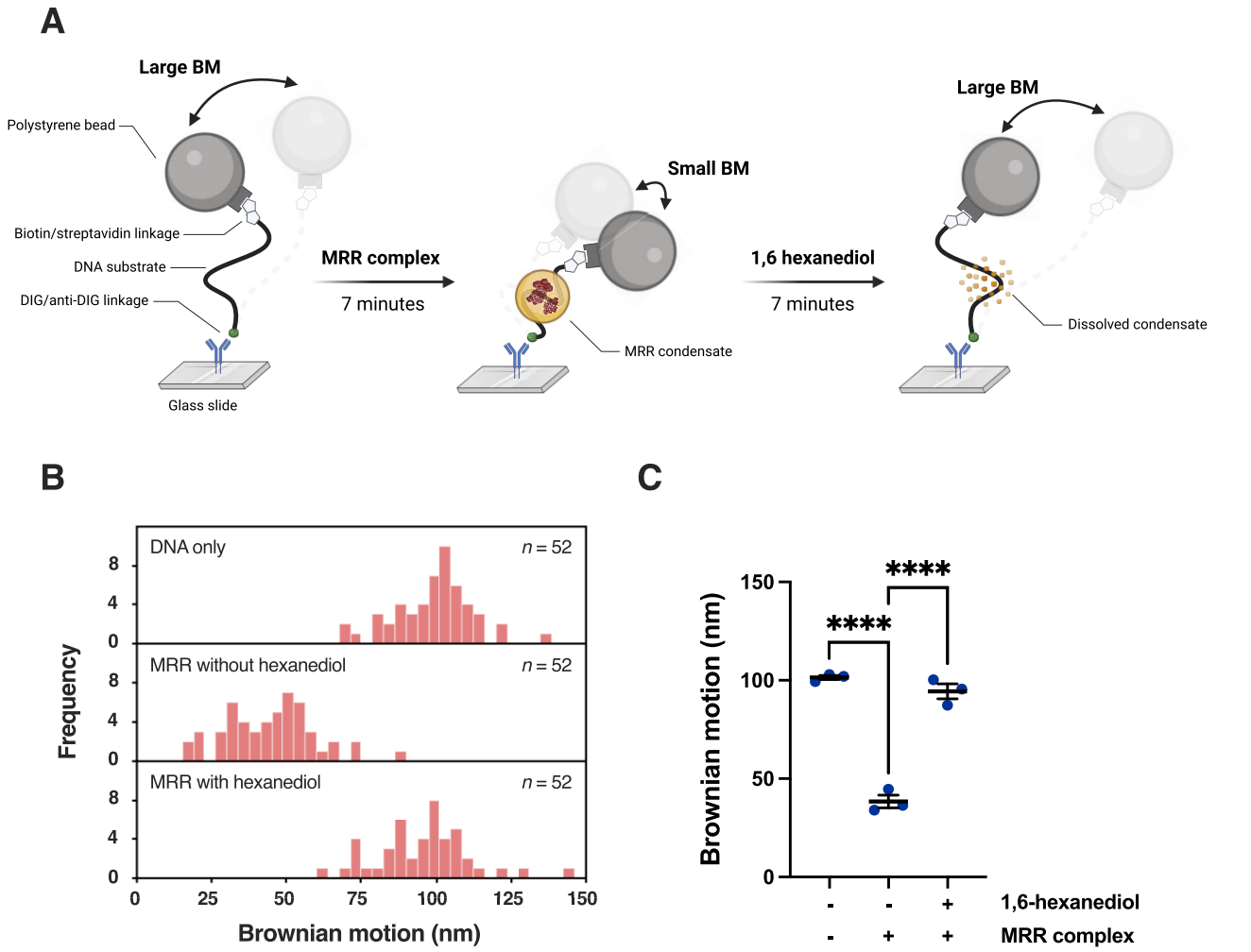

Figure 4. MRR compacts duplex DNA. (**A**) Schematic of the single-molecule TPM experiment. BM and DIG represent Brownian motion and digoxigenin, respectively. (**B**) Representative distribution of median BM of the DNA-tethered beads under different conditions. *n* is the number of DNA molecules measured. Median BM values were taken from 500 frames. (**C**) Mean of the median BM of the DNA-tethered beads under different conditions. Data are shown as mean ± SEM from three independent experiments. Statistical significance was determined using one-way ANOVA with Šidák's post hoc test. ****$p < 0.0001$.

mutations that modestly reduced DSB levels, meiotic gene conversion, and crossovers. Lysine (K) or arginine (R) residues were substituted with glutamic acid (E) in these mutant lines—*rec27-238* (K28E), *rec27-239* (R32E), and *rec27-240* (K36E), with these K and R sites being closely spaced and conserved in other *Schizosaccharomyces* spp. (Fig. 5A). Consequently, we surmised that these and neighboring positively-charged residues of Rec27 (Fig. 5A) contribute to the DNA binding activity of the MRR complex. Based on this speculation, we mutated these putative DNA-interacting residues (K28E, R32E, R33E, K35E, and K36E) and purified the resulting mutant variant, hereafter referred to as the MRR-5E complex. Of note, substituting the five negatively charged amino acid residues resulted in a considerable decrease in the electrophoretic mobility of the 5E variant compared to that of wild-type Rec27 (Fig. 5B). These protein complexes were subjected to CD spectroscopy to exclude severe structural alteration between wild-type MRR and the MRR-5E complex. As shown in Supplementary Fig. S5, the mutant complex has a global protein structure indistinguishable from that of its wild-type counterpart. A mobility shift assay indicated that these amino acid substitutions yielded a mutant that was defective in DNA binding (Fig. 5C).

Next, we endeavored to test condensate assembly using this mutant variant. For the purified sfGFP-conjugated MRR-5E complex (Supplementary Fig. S6A and B), no condensates formed in the presence of duplex DNA, even with a protein concentration four-fold higher (20 μM) than that used for the wild-type MRR complex or, unexpectedly, even in the absence of duplex DNA (Fig. 5D). We also conducted a TPM experiment to test this mutant variant's capability to compact DNA. There was no significant difference in BM values between the groups with or without the MRR-5E complex, even with a protein concentration two-fold higher (2.64 μM) than that used for the wild-type MRR complex or following 1-hour incubation (Supplementary Fig. S7).

To determine if these point mutations in Rec27 affect *S. pombe* meiotic recombination, we generated a mutant strain that harbors the five substituted residues (5E) in Rec27 (*rec27-283*) and analyzed its intragenic and intergenic (i.e., gene conversion and crossover) recombinant frequencies and DSB

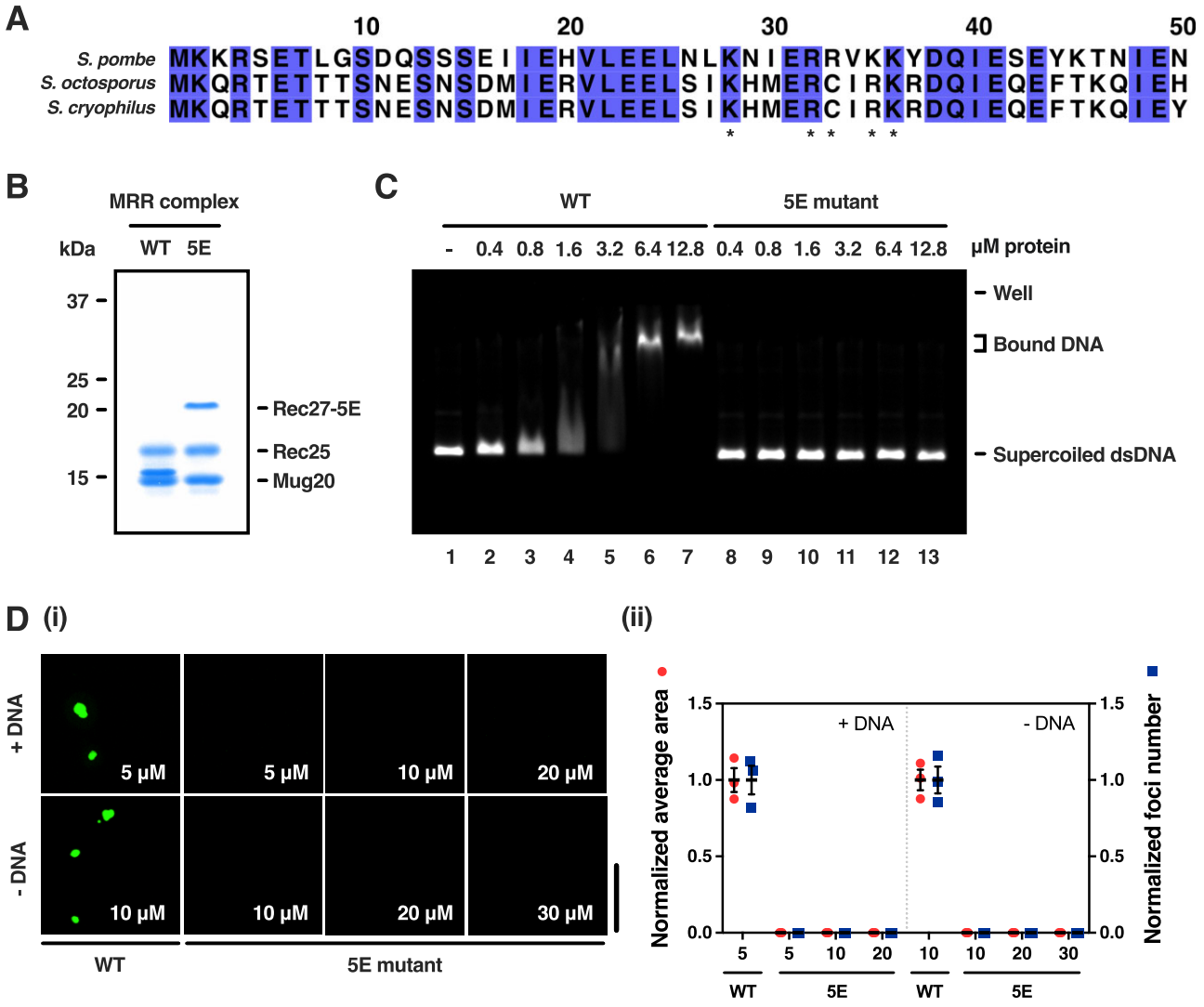

Figure 5. Basic residues in Rec27 account for DNA binding activity and condensate assembly. (**A**) Amino acid sequence alignment of the 50 N-terminal residues of Rec27 from different *Schizosaccharomyces* spp. was performed using Clustal Omega [77]. Identical amino acids are shaded. Five conserved lysine (K) or arginine (R) residues were mutated to glutamic acid (E), which are indicated by asterisks. (**B**) SDS-PAGE of the purified MRR-5E complex (3 μg was loaded). (**C**) The indicated concentrations of the WT MRR complex and its 5E mutant variant were incubated with 3-kb supercoiled plasmid DNA substrates. Binding was analyzed by an electrophoretic mobility shift assay. (**D**) (i) Representative micrographs of WT MRR complex and its 5E mutant variant with different concentrations in the presence or absence of supercoiled plasmid DNA. (ii) Normalized foci number and average foci area from different protein concentrations (μM). Quantification data were normalized to the mean of the WT MRR complex. Data are shown as mean ± SEM from three independent replicates. The scale bar is 10 μm. DNA was used at a concentration of 5 nM molecules.

formation at hotspots. Compared to wild-type cells, the frequency of gene conversion at the *ade6-M26* hotspot [63, 64] was reduced 42-fold (*ade6-M26* × *52*) for the *rec27-283* (5E) line, and crossovers in the *ade6–arg1* and *ade6–ura4* intervals were reduced by factors of 15 and 10 (Fig. 6A and B, Supplementary Table S3), respectively, which are close to *rec27*Δ levels.

Acting as a DSB hotspot-associated protein vital for meiotic recombination, such deficiency observed for the *rec27-283* (5E) mutant could be caused by a failure of DSB formation. Thus, we assayed DSB formation at several hotspots, including the well-studied *ade6-3049*, *mbs1*, and *mbs2* sites [48, 65]. Cells were induced to enter highly synchronous meiosis by inactivating the ATP analog-sensitive mutant of the Pat1 protein kinase (*pat1-as1*) in the *rad50S* mutant to accumulate meiotic DNA breaks [48, 66]. As shown in Fig. 6C and Supplementary Table S4, frequencies declined in parallel with the reductions in recombinant frequencies, and they were almost abolished to *rec27*Δ levels at the tested hotspots.

In addition, we observed the nuclear structure of LinE proteins in the horsetail stage using structured illumination fluorescence microscopy. Rec25–GFP formed only a few punctate foci in the *rec27-283* (5E) line instead of the typical elongated linear structures of wild-type cells (Fig. 6D). We further treated wild-type and *rec27-283* (5E) cells with 1,6-hexanediol and observed the punctate foci of Rec25–GFP in the cell nuclei. After treatment, Rec25–GFP in wild-type cells lost its linear structure, whereas the punctate Rec25–GFP foci in the *rec27-283* (5E) cells remained (Supplementary Fig. S8), indicating that the aberrant LinE structures in the *rec27-283* (5E) mutant cells are not sensitive to 1,6-hexanediol.

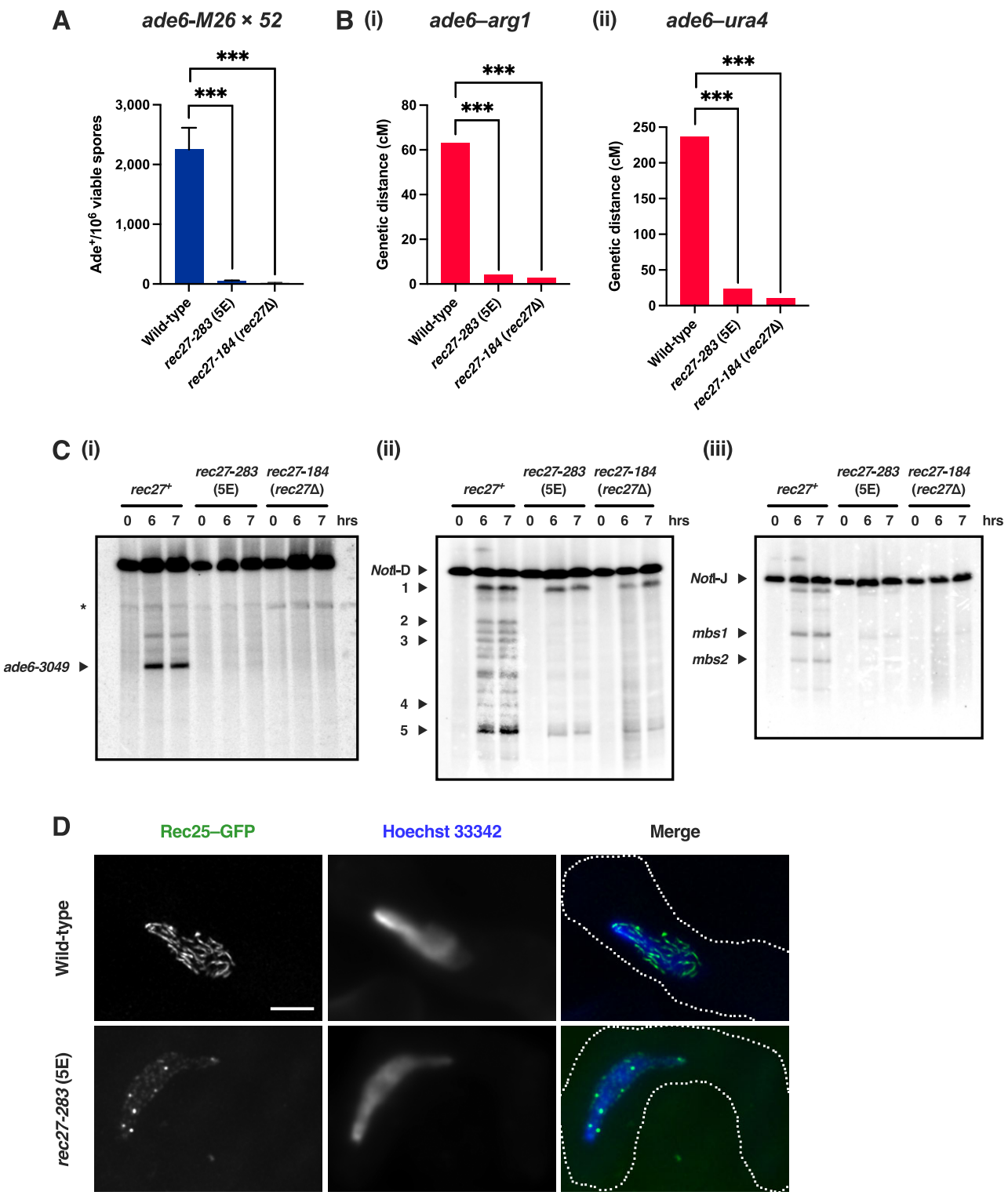

Figure 6. The *rec27-283* (5E) mutant exhibits reduced meiotic recombination, DNA DSB frequency, and abnormal linear structures. (**A**–**B**) Frequencies of meiotic (**A**) gene conversion to *ade6*$^+$ at the *ade6* locus and (**B**) cross-over in the (i) *ade6–arg1* and (ii) *ade6–ura4* intervals in *rec27* mutants. Data are from Supplementary Table S3. Statistical significance was determined using the unpaired *t*-test. ***$p < 0.001$. (**C**) (i) DSBs at the *ade6* locus on chromosome III. The black triangle shows breakage at the *ade6-3049* hotspot, and the asterisk shows a meiosis-independent DSB site. DSBs in the (ii) *Not*I-D and (iii) *Not*I-J regions on chromosome I. DSB frequencies of five hotspots in (ii) *Not*I-D [1–5] and two hotspots in (iii) *Not*I-J (*mbs1* and *mbs2*) are quantified in Supplementary Table S4. Meiotically induced cells of WT, *rec27-283* (5E), and *rec27-184* (*rec27*Δ) were collected at the indicated time points. DNA was prepared, digested with (i) *Pme*I or (ii and iii) *Not*I, and analyzed by gel electrophoresis and Southern blot hybridization with the indicated DNA probes previously described [47]. (**D**) Rec25–GFP protein was observed in *rec27-283* (5E) cells of h^{90} (homothallic) strains using live-cell super-resolution fluorescence microscopy at 25°C. Hoechst 33342 stains nuclear DNA. Each image is representative of at least 20 cells examined. Images show the maximal projection of the entire Z-stack of image sections. Dotted lines outline the cells. The scale bar is 2 μm.

Overall, these clustered missense mutations conferred defects in both DNA-binding activity and condensate assembly *in vitro*. *In vivo*, they elicited defective meiotic DSB formation, recombination, and LinE structures. These outcomes indicate that the DNA-binding activity of the MRR complex is vital for *S. pombe* DSB generation, and, in turn, it is likely that condensate formation itself is essential for the biological functions of the MRR complex.

Formation of the MRR complex is required for DNA binding activity and condensate assembly

Based on the results of previous genetic research [8, 38] and our current findings, we speculated that Rec27 might be the predominant MRR subunit that binds duplex DNA. To analyze the DNA binding ability of Rec27, we purified untagged Rec27 according to an identical purification protocol as described above for the MRR complex (Fig. 1C and Supplementary Fig. S6D, see also Materials and Methods). Surprisingly, Rec27 did not bind the DNA substrates even at a protein concentration four-fold higher (20 μM) than that needed for the MRR complex to bind DNA (Fig. 7A). To further clarify the role of DNA binding by the MRR complex, we also purified Rec25 and Mug20 (Supplementary Fig. S6E) and performed a mobility shift assay. Neither Rec25 nor Mug20 yielded mobility shifts compared to the wild-type MRR complex (Fig. 7A). We reconstituted the protein complex by co-incubating these three proteins, and it bound DNA substrates in a mobility shift assay (Fig. 7B). Notably, we also purified the *rec27-283* (5E) mutant protein (Supplementary Fig. S6E) as a negative control and repeated protein complex reconstitution as for subsequent assays, yet no DNA binding by the MRR-5E complex was observed (Fig. 7B, compare lanes 3–6 with 7–10). Thus, Rec27 primarily accounts for the DNA binding activity of the MRR complex, but Rec25 and Mug20 are also indispensable for the DNA binding activity of Rec27. In parallel, regardless of the presence of duplex DNA, Rec27 alone did not assemble any condensates, even at high protein concentrations (Fig. 7C), most likely due to disruption of the multivalency arising from protein-protein interactions. Collectively, our findings are evidence of the importance of the MRR complex's intactness and provide a feasible explanation for the interdependency of these three proteins *in vivo* [8].

Discussion

LinE proteins—Mug20, Rec25, and Rec27—are enriched at hotspots with unprecedented specificity and are required for high-level DSB formation at most hotspots and meiotic recombination in *S. pombe* [8]. Using our highly purified proteins, we show that they form an intact complex that binds DNA and forms phase-separated condensates. Our single-molecule TPM analyses further reveal that these condensates significantly compact DNA. Furthermore, individually, none of the three proteins binds DNA or assembles condensates, underlining the importance of protein complex intactness and explaining the interdependency of these proteins.

During meiotic recombination, DSB formation at hotspots needs to be strictly regulated, both numerically and spatially. The activity of hotspots is limited via hotspot competition since the DSB activity of a hotspot is reduced in the presence of neighboring strong hotspots [49, 58, 59]. Previous studies have proposed a DSB hotspot clustering model to explain the molecular mechanism of hotspot competition and related interference [40, 49], representing a long-standing and hotly debated topic in meiosis. Our findings of MRR-dependent condensation provide fundamental support for this model from biophysical and biochemical perspectives. This model suggests that competition occurs during DSB formation, not during loading of the protein complex at the hotspots, which might be mediated by other factors, such as cohesin or condensin, or by self-loading [40, 49]. In *S. pombe* meiotic cells, cohesin and condensin, respectively, form topologically associating domains (TADs) of 50–100 and 300–500 kb that are similar to the reported distance (~200 kb) of hotspot competition [49, 67]. In the context of self-loading of the MRR complex, proteins are nucleated in a microenvironment with poor diffusion because of their low-dynamic material properties, leading to local depletion of the complex, thereby reducing the probability of neighboring nucleation events. This proposed mechanism is similar to that described for the Spo11-accessory proteins Rec114–Mei4 and Mer2 in *S. cerevisiae* [68]. In either scenario, following loading of the MRR complex, protein-protein and protein-DNA multivalent interactions induce the assembly of nucleoprotein condensates, which compact DNA and cluster neighboring hotspots (Supplementary Fig. S9). However, the factors that determine the preferential loading sites of the MRR complex (e.g., sequence specificity, transcription factors, or higher-order chromosomal structure [16–26]) remain to be determined. Overall, our findings provide important molecular insights into how these LinEs spatially and numerically regulate DSB formation, though further investigations of the loading mechanism and the potential loader are required.

Biomolecular condensates form interfaces with surrounding cytoplasm and cellular structures, such as membranes, the cytoskeleton, and chromosomes. The resulting interfacial tension, or capillary force, impacts the local mechanics, cellular morphology, and organization of chromosomes [69]. There is a growing awareness of the importance of nuclear condensate capillarity, such as how interfacial interactions within transcription factor–chromatin condensates mediate DNA remodeling [60, 69, 70], and how the forces generated by meiosis-associated protein condensates on chromosomes regulate the pattern of recombination events [71]. A recent study revealed that a complex comprised of the C-terminus of Rec114 and the N-terminus of Mei4 of *S. cerevisiae* (RM minimal complex) bridges multiple DNA duplexes and generates forces that condense DNA through long-range interactions [71]. Likewise, our single-molecule experiment has uncovered MRR condensate-mediated DNA compaction (Fig. 4), which might also arise from the capillary forces generated by the nucleoprotein condensates. Therefore, we propose that the MRR complex may be another example of reconciling condensate capillarity with meiotic chromosome dynamics, which should be further experimentally validated.

During prophase I, LinE proteins form two nuclear structures, i.e., punctate and linear structures, and undergo a punctate-to-linear-to-punctate configurational transition that was proposed to align with DSB formation, chromosome pairing and DSB repair [72], before disassembling in advance of the first meiotic division [34]. Disruption of the intracellular linear structures by 1,6-hexanediol treatment indicates that the phase separation property of the purified MRR complex assessed herein not only contributes to hotspot activation but also to chromosome pairing, which is governed by the synap-

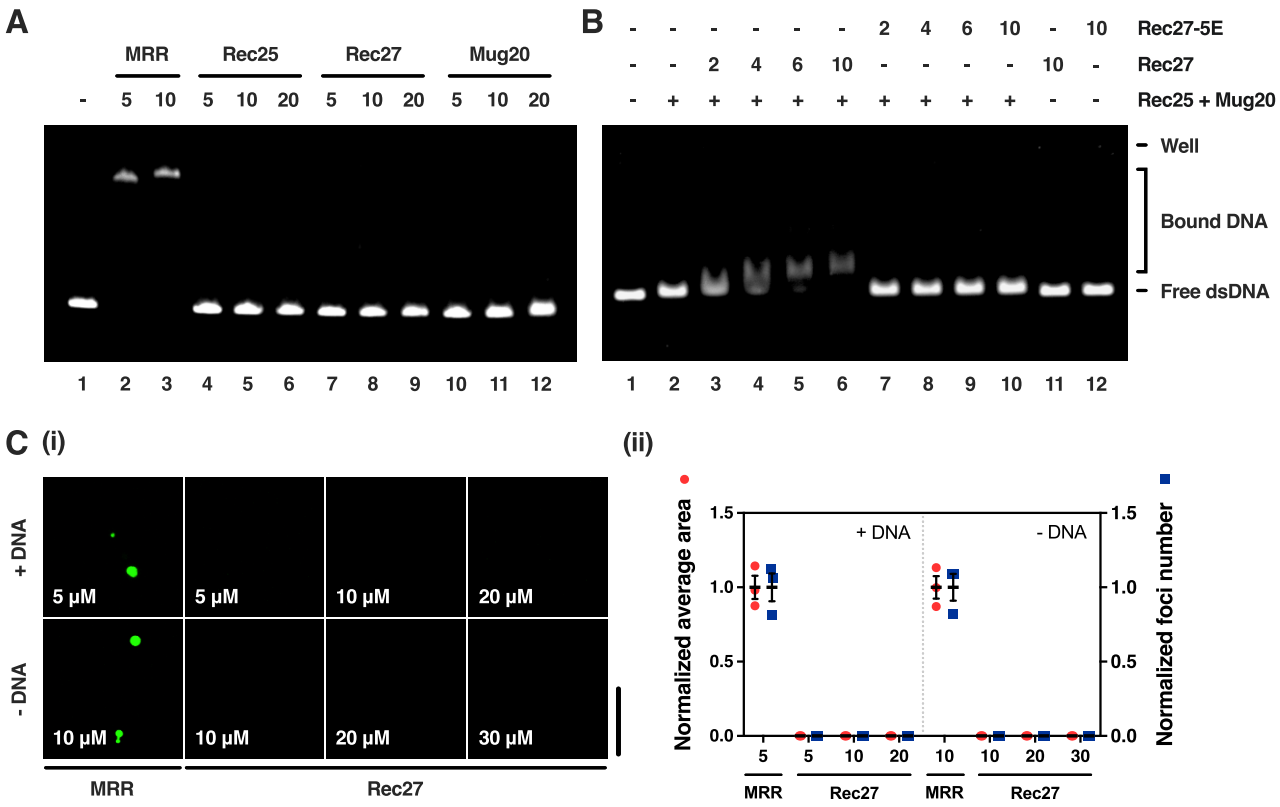

Figure 7. Individual Mug20, Rec25, and Rec27 proteins neither bind DNA nor assemble condensates. (**A**) The indicated concentrations (μM) of the WT MRR complex, Rec25, Rec27, and Mug20, were incubated with 3-kb supercoiled plasmid DNA substrates. (**B**) The indicated concentrations (μM) of Rec27 and Rec27-5E proteins were incubated with 10 μM Rec25 and Mug20 and supercoiled plasmid DNA. (**C**) (i) Representative micrographs of the WT MRR complex and the Rec27 protein with different concentrations in the presence or absence of 3-kb supercoiled DNA. (ii) Normalized foci number and average foci area from different protein concentrations. Quantification data were normalized to the mean of the WT MRR complex. Data are shown as mean ± SEM from three independent replicates. DNA was used at a concentration of 5 nM molecules.

tonemal complex in most eukaryotes. Typically, synaptonemal complex proteins self-assemble on chromosome axes and interact with each other in a coiled-coil manner, forming a filamentous and stable structure [73, 74]. Synaptonemal complex proteins assemble with liquid crystalline properties in *C. elegans*, *S. cerevisiae*, and the fruit fly *Drosophila melanogaster* [37]. This relatively more stable and less dynamic state resembles the material properties observed for the *S. pombe* MRR complex (Supplementary Fig. S4A). Interestingly, we have revealed the oligomeric nature of the MRR complex through size exclusion chromatography (Supplementary Fig. S1B) and predicted it to form a coiled-coil structure (Supplementary Fig. S10). These findings support the view that synaptonemal complex and LinE proteins display evolutionarily conserved structures, properties, and functions [27, 28].

The MRR complex functions with another LinE protein, Rec10, in meiotic recombination, which has been reported previously to interact with Rec25 [29]. Compared with the MRR complex, Rec10 binds chromosomes nearly uniformly, except for a modest preferential localization at strong hotspots [8]. Loss of Rec10 causes abnormal LinE structure formation of Mug20, Rec25, and Rec27, and it also abolishes meiotic DSB formation and meiotic recombination, i.e., the phenotype of the *rec12*Δ mutant [8, 30, 38, 75]. Furthermore, a recent study demonstrated that Rec10 coordinates the nuclear entry of the MRR complex via its bipartite nuclear localization signal [76]. Interestingly, Hyppa *et al.* [40] observed that both intragenic and intergenic recombinant frequencies at an artificial hotspot (chromosomal *lacO* array with a Mug20–NLS–LacI fusion protein) were strongly reduced in the *rec10*Δ strain, implying that Rec10 exerts an additional function at DSB hotspots other than escorting the MRR complex into the cell nucleus and perhaps localizing the MRR complex to a hotspot. Therefore, the mechanistic role of Rec10 and how it coordinates with the MRR complex in meiotic DSB formation warrants further study. The protein purification procedures and biochemical analyses developed herein should facilitate future efforts to delineate the basis for the functional interactions between Rec10 and the MRR complex.

Acknowledgements

We thank Randy Hyppa (Fred Hutchinson Cancer Center, USA) for valuable help and insightful conversations regarding this study. We thank the Bio-Imaging Core Facility at the Institute of Biological Chemistry, Academia Sinica, for technical support in FRAP data acquisition. We also acknowledge the Biophysics Core Facility, funded by the Academia Sinica Core Facility and Innovative Instrument Project (AS-CFII-101–201), for collecting data from CD spectroscopy and mass photometry. The graphical abstract and schematic diagrams in Fig. 4A and Supplementary Fig. S9 were created in BioRender [Wang, F. (2025) https://BioRender.com/v10y283].

Author contributions: M.F.W.: Conceptualization, Methodology, Investigation, Formal analysis, Visualization, Writing – original draft, Writing – review & editing, and Project administration. M.-Y.L.: Conceptualization, Methodology, and Investigation. Y.-C.Y.: Investigation. Y.-C.C.: Investigation, Formal analysis, and Visualization. C.-Y.T.: Methodology, Investigation, Formal analysis, Visualization, and Writing – original draft. M.-C.N.B.: Investigation. L.M.: Investigation. S.-W.L.: Investigation, Formal analysis, and Visualization. H.-W.L.: Methodology, Supervision, and Funding acquisition. G.R.S.: Methodology, Writing – review & editing, Supervision, and Funding acquisition. P.C.: Conceptualization, Methodology, Writing – review & editing, Project administration, Supervision, and Funding acquisition.

Supplementary data

Supplementary data is available at NAR online.

Conflict of interest

The authors declare no competing interests.

Funding

This work was supported by the National Science and Technology Council (Ministry of Science and Technology, MOST, before July 2022) [MOST 111-2311-B-002-006-MY3 and NSTC 112-2326-B-002-008 to P.C., MOST 110-2113-M-002-020-MY3 to H.-W.L.]; the National Institutes of Health of the United States of America [NIH R35 GM118120 to G.R.S. and NIH P30 CA015704 to the Cellular Imaging Shared Resource, RRID:SCR_022609, of the Fred Hutchinson/University of Washington/Seattle Children's Cancer Consortium]. Funding to pay the Open Access publication charges for this article was provided by the National Science and Technology Council.

Data availability

The relevant data are described in the Supplementary Information. Other additional data that support the findings of this study are available from the authors upon reasonable request.

References

1. Zickler D, Kleckner N. Meiotic chromosomes: integrating structure and function. *Mol Syst Biol* 1999;**33**:10952–7. https://doi.org/10.1146/annurev.genet.33.1.603
2. Marston AL, Amon A. Meiosis: cell-cycle controls shuffle and deal. *Nat Rev Mol Cell Biol* 2004;**5**:983–97. https://doi.org/10.1038/nrm1526
3. Keeney S, Giroux CN, Kleckner N. Meiosis-specific DNA double-strand breaks are catalyzed by Spo11, a member of a widely conserved protein family. *Cell* 1997;**88**:375–84. https://doi.org/10.1016/S0092-8674(00)81876-0
4. Baudat F, Manova K, Yuen JP *et al.* Chromosome synapsis defects and sexually dimorphic meiotic progression in mice lacking Spo11. *Mol Cell* 2000;**6**:989–98. https://doi.org/10.1016/S1097-2765(00)00098-8
5. Cervantes MD, Farah JA, Smith GR. Meiotic DNA breaks associated with recombination in *S. pombe*. *Mol Cell* 2000;**5**:883–8. https://doi.org/10.1016/S1097-2765(00)80328-7
6. Dernburg AF, McDonald K, Moulder G *et al.* Meiotic recombination in *C. elegans* initiates by a conserved mechanism and is dispensable for homologous chromosome synapsis. *Cell* 1998;**94**:387–98. https://doi.org/10.1016/S0092-8674(00)81481-6
7. Nambiar M, Chuang YC, Smith GR. Distributing meiotic crossovers for optimal fertility and evolution. *DNA Repair (Amst)* 2019;**81**:102648. https://doi.org/10.1016/j.dnarep.2019.102648
8. Fowler KR, Gutierrez-Velasco S, Martin-Castellanos C *et al.* Protein determinants of meiotic DNA break hot spots. *Mol Cell* 2013;**49**:983–96. https://doi.org/10.1016/j.molcel.2013.01.008
9. Fowler KR, Sasaki M, Milman N *et al.* Evolutionarily diverse determinants of meiotic DNA break and recombination landscapes across the genome. *Genome Res* 2014;**24**:1650–64. https://doi.org/10.1101/gr.172122.114
10. Pan J, Sasaki M, Kniewel R *et al.* A hierarchical combination of factors shapes the genome-wide topography of yeast meiotic recombination initiation. *Cell* 2011;**144**:719–31. https://doi.org/10.1016/j.cell.2011.02.009
11. Lange J, Yamada S, Tischfield SE *et al.* The landscape of mouse meiotic double-strand break formation, processing, and repair. *Cell* 2016;**167**:695–708. https://doi.org/10.1016/j.cell.2016.09.035
12. Lam I, Keeney S. Nonparadoxical evolutionary stability of the recombination initiation landscape in yeast. *Science* 2015;**350**:932–7. https://doi.org/10.1126/science.aad0814
13. Mohibullah N, Keeney S. Numerical and spatial patterning of yeast meiotic DNA breaks by Tel1. *Genome Res.* 2017;**27**:278–88. https://doi.org/10.1101/gr.213587.116
14. Pratto F, Brick K, Khil P *et al.* DNA recombination. Recombination initiation maps of individual human genomes. *Science.* 2014;**346**:1256442. https://doi.org/10.1126/science.1256442
15. Mihola O, Landa V, Pratto F *et al.* Rat PRDM9 shapes recombination landscapes, duration of meiosis, gametogenesis, and age of fertility. *BMC Biol* 2021;**19**:86. https://doi.org/10.1186/s12915-021-01017-0
16. Steiner WW, Davidow PA, Bagshaw AT. Important characteristics of sequence-specific recombination hotspots in *Schizosaccharomyces pombe*. *Genetics* 2011;**187**:385–96. https://doi.org/10.1534/genetics.110.124636
17. Wahls WP, Davidson MK. Discrete DNA sites regulate global distribution of meiotic recombination. *Trends Genet* 2010;**26**:202–8. https://doi.org/10.1016/j.tig.2010.02.003
18. Wu TC, Lichten M. Meiosis-induced double-strand break sites determined by yeast chromatin structure. *Science* 1994;**263**:515–8. https://doi.org/10.1126/science.8290959
19. Choi K, Zhao X, Kelly KA *et al. Arabidopsis* meiotic crossover hot spots overlap with H2A.Z nucleosomes at gene promoters. *Nat Genet* 2013;**45**:1327–36. https://doi.org/10.1038/ng.2766
20. Choi K, Zhao X, Tock AJ *et al.* Nucleosomes and DNA methylation shape meiotic DSB frequency in *Arabidopsis thaliana* transposons and gene regulatory regions. *Genome Res* 2018;**28**:532–46. https://doi.org/10.1101/gr.225599.117
21. de Castro E, Soriano I, Marin L *et al.* Nucleosomal organization of replication origins and meiotic recombination hotspots in fission yeast. *EMBO J* 2012;**31**:124–37. https://doi.org/10.1038/emboj.2011.350
22. Borde V, Robine N, Lin W *et al.* Histone H3 lysine 4 trimethylation marks meiotic recombination initiation sites. *EMBO J* 2009;**28**:99–111. https://doi.org/10.1038/emboj.2008.257
23. Grey C, Barthes P, Friec C-L *et al.* Mouse PRDM9 DNA-binding specificity determines sites of histone H3 lysine 4 trimethylation for initiation of meiotic recombination. *PLoS*

Biol 2011;**9**:e1001176. https://doi.org/10.1371/journal.pbio.1001176
24. Smagulova F, Gregoretti IV, Brick K *et al.* Genome-wide analysis reveals novel molecular features of mouse recombination hotspots. *Nature* 2011;**472**:375–8. https://doi.org/10.1038/nature09869
25. Yamada S, Ohta K, Yamada T. Acetylated histone H3K9 is associated with meiotic recombination hotspots, and plays a role in recombination redundantly with other factors including the H3K4 methylase Set1 in fission yeast. *Nucleic Acids Res* 2013;**41**:3504–17. https://doi.org/10.1093/nar/gkt049
26. Yamada S, Kugou K, Ding DQ *et al.* The histone variant H2A.Z promotes initiation of meiotic recombination in fission yeast. *Nucleic Acids Res* 2018;**46**:609–20. https://doi.org/10.1093/nar/gkx1110
27. Lorenz A, Wells JL, Pryce DW *et al. S. pombe* meiotic linear elements contain proteins related to synaptonemal complex components. *J Cell Sci* 2004;**117**:3343–51. https://doi.org/10.1242/jcs.01203
28. Loidl J. *S. pombe* linear elements: the modest cousins of synaptonemal complexes. *Chromosoma* 2006;**115**:260–71. https://doi.org/10.1007/s00412-006-0047-7
29. Estreicher A, Lorenz A, Loidl J. Mug20, a novel protein associated with linear elements in fission yeast meiosis. *Curr Genet* 2012;**58**:119–27. https://doi.org/10.1007/s00294-012-0369-3
30. Davis L, Rozalen AE, Moreno S *et al.* Rec25 and Rec27, novel linear-element components, link cohesin to meiotic DNA breakage and recombination. *Curr Biol* 2008;**18**:849–54. https://doi.org/10.1016/j.cub.2008.05.025
31. Simonis N, Rual JF, Carvunis AR *et al.* Empirically controlled mapping of the *Caenorhabditis elegans* protein-protein interactome network. *Nat Methods* 2009;**6**:47–54. https://doi.org/10.1038/nmeth.1279
32. Ding DQ, Yamamoto A, Haraguchi T *et al.* Dynamics of homologous chromosome pairing during meiotic prophase in fission yeast. *Dev Cell* 2004;**6**:329–41. https://doi.org/10.1016/S1534-5807(04)00059-0
33. Bahler J, Wyler T, Loidl J *et al.* Unusual nuclear structures in meiotic prophase of fission yeast: a cytological analysis. *J Cell Biol* 1993;**121**:241–56. https://doi.org/10.1083/jcb.121.2.241
34. Chuang YC, Smith GR. Dynamic configurations of meiotic DNA-break hotspot determinant proteins. *J Cell Sci* 2022;**135**:jcs259061. https://doi.org/10.1242/jcs.259061
35. Kroschwald S, Maharana S, Simon A. Hexanediol: a chemical probe to investigate the material properties of membrane-less compartments. *Matters* 2017;**3**:e201702000010. https://doi.org/10.19185/matters.201702000010
36. Shin Y, Brangwynne CP. Liquid phase condensation in cell physiology and disease. *Science* 2017;**357**:eaaf4382. https://doi.org/10.1126/science.aaf4382
37. Rog O, Kohler S, Dernburg AF. The synaptonemal complex has liquid crystalline properties and spatially regulates meiotic recombination factors. *eLife* 2017;**6**:e21455. https://doi.org/10.7554/eLife.21455
38. Ma L, Fowler KR, Martin-Castellanos C *et al.* Functional organization of protein determinants of meiotic DNA break hotspots. *Sci Rep* 2017;**7**:1393. https://doi.org/10.1038/s41598-017-00742-3
39. Martin-Castellanos C, Blanco M, Rozalen AE *et al.* A large-scale screen in S. pombe identifies seven novel genes required for critical meiotic events. *Curr Biol* 2005;**15**:2056–62. https://doi.org/10.1016/j.cub.2005.10.038
40. Hyppa RW, Cho JD, Nambiar M *et al.* Redirecting meiotic DNA break hotspot determinant proteins alters localized spatial control of DNA break formation and repair. *Nucleic Acids Res* 2022;**50**:899–914. https://doi.org/10.1093/nar/gkab1253
41. Smith GR. Genetics analysis of meiotic recombination in *Schizosaccharomyces pombe*. In: Keeney S (ed.), *Meiosis: Volume 1, Molecular and Genetic Methods*. Totowa, NJ: Humana Press, pp. 2009, 65–76.
42. Pedelacq JD, Cabantous S, Tran T *et al.* Engineering and characterization of a superfolder green fluorescent protein. *Nat Biotechnol* 2006;**24**:79–88. https://doi.org/10.1038/nbt1172
43. Nishihara K, Kanemori M, Yanagi H *et al.* Overexpression of trigger factor prevents aggregation of recombinant proteins in *Escherichia coli*. *Appl Environ Microb* 2000;**66**:884–9. https://doi.org/10.1128/AEM.66.3.884-889.2000
44. Wu D, Piszczek G. Standard protocol for mass photometry experiments. *Eur Biophys J* 2021;**50**:403–9. https://doi.org/10.1007/s00249-021-01513-9
45. Schindelin J, Arganda-Carreras I, Frise E *et al.* Fiji: an open-source platform for biological-image analysis. *Nat Methods* 2012;**9**:676–82. https://doi.org/10.1038/nmeth.2019
46. Lu CH, Lan WH, Li HW. Single-molecule tethered particle motion studies on the DNA recombinase filament assembly and disassembly. *Methods Mol Biol* 2021;**2281**:135–49. https://doi.org/10.1007/978-1-0716-1290-3_8
47. Hyppa RW, Smith GR. Using *Schizosaccharomyces pombe* meiosis to analyze DNA recombination intermediates. *Methods Mol Biol* 2009;**557**:235–52. https://doi.org/10.1007/978-1-59745-527-5_15
48. Young JA, Schreckhise RW, Steiner WW *et al.* Meiotic recombination remote from prominent DNA break sites in *S. pombe*. *Mol Cell* 2002;**9**:253–63. https://doi.org/10.1016/S1097-2765(02)00452-5
49. Fowler KR, Hyppa RW, Cromie GA *et al.* Physical basis for long-distance communication along meiotic chromosomes. *Proc Natl Acad Sci USA* 2018;**115**:E9333–42. https://doi.org/10.1073/pnas.1801920115
50. Jumper J, Evans R, Pritzel A *et al.* Highly accurate protein structure prediction with AlphaFold. *Nature* 2021;**596**:583–9. https://doi.org/10.1038/s41586-021-03819-2
51. Mirdita M, Schutze K, Moriwaki Y *et al.* ColabFold: making protein folding accessible to all. *Nat Methods* 2022;**19**:679–82. https://doi.org/10.1038/s41592-022-01488-1
52. Wright PE, Dyson HJ. Intrinsically disordered proteins in cellular signalling and regulation. *Nat Rev Mol Cell Biol* 2015;**16**:18–29. https://doi.org/10.1038/nrm3920
53. van der Lee R, Buljan M, Lang B *et al.* Classification of intrinsically disordered regions and proteins. *Chem Rev* 2014;**114**:6589–631. https://doi.org/10.1021/cr400525m
54. King JT, Shakya A. Phase separation of DNA: from past to present. *Biophys J* 2021;**120**:1139–49. https://doi.org/10.1016/j.bpj.2021.01.033
55. Ghosh A, Mazarakos K, Zhou HX. Three archetypical classes of macromolecular regulators of protein liquid-liquid phase separation. *Proc Natl Acad Sci USA* 2019;**116**:19474–83. https://doi.org/10.1073/pnas.1907849116
56. Hatos A, Tosatto SCE, Vendruscolo M *et al.* FuzDrop on AlphaFold: visualizing the sequence-dependent propensity of liquid-liquid phase separation and aggregation of proteins. *Nucleic Acids Res* 2022;**50**:W337–344. https://doi.org/10.1093/nar/gkac386
57. Jawerth L, Fischer-Friedrich E, Saha S *et al.* Protein condensates as aging Maxwell fluids. *Science* 2020;**370**:1317–23. https://doi.org/10.1126/science.aaw4951
58. Fan QQ, Xu F, White MA *et al.* Competition between adjacent meiotic recombination hotspots in the yeast *Saccharomyces cerevisiae*. *Genetics* 1997;**145**:661–70. https://doi.org/10.1093/genetics/145.3.661
59. Wu TC, Lichten M. Factors that affect the location and frequency of meiosis-induced double-strand breaks in *Saccharomyces cerevisiae*. *Genetics* 1995;**140**:55–66. https://doi.org/10.1093/genetics/140.1.55
60. Quail T, Golfier S, Elsner M *et al.* Force generation by protein–DNA co-condensation. *Nat Phys* 2021;**17**:1007–12. https://doi.org/10.1038/s41567-021-01285-1

61. Schafer DA, Gelles J, Sheetz MP *et al.* Transcription by single molecules of RNA polymerase observed by light microscopy. *Nature* 1991;**352**:444–8. https://doi.org/10.1038/352444a0
62. Lin YY, Li MH, Chang YC *et al.* Dynamic DNA shortening by telomere-binding protein Cdc13. *J Am Chem Soc* 2021;**143**:5815–25. https://doi.org/10.1021/jacs.1c00820
63. Ponticelli AS, Sena EP, Smith GR. Genetic and physical analysis of the M26 recombination hotspot of *Schizosaccharomyces pombe*. *Genetics* 1988;**119**:491–7. https://doi.org/10.1093/genetics/119.3.491
64. Steiner WW, Schreckhise RW, Smith GR. Meiotic DNA breaks at the *S. pombe* recombination hot spot *M26*. *Mol Cell* 2002;**9**:847–55. https://doi.org/10.1016/S1097-2765(02)00489-6
65. Steiner WW, Smith GR. Optimizing the nucleotide sequence of a meiotic recombination hotspot in *Schizosaccharomyces pombe*. *Genetics* 2005;**169**:1973–83. https://doi.org/10.1534/genetics.104.039230
66. Guerra-Moreno A, Alves-Rodrigues I, Hidalgo E *et al.* Chemical genetic induction of meiosis in *Schizosaccharomyces pombe*. *Cell Cycle* 2012;**11**:1621–5. https://doi.org/10.4161/cc.20051
67. Kim KD, Tanizawa H, Iwasaki O *et al.* Transcription factors mediate condensin recruitment and global chromosomal organization in fission yeast. *Nat Genet* 2016;**48**:1242–52. https://doi.org/10.1038/ng.3647
68. Claeys Bouuaert C, Pu S, Wang J *et al.* DNA-driven condensation assembles the meiotic DNA break machinery. *Nature* 2021;**592**:144–9. https://doi.org/10.1038/s41586-021-03374-w
69. Gouveia B, Kim Y, Shaevitz JW *et al.* Capillary forces generated by biomolecular condensates. *Nature* 2022;**609**:255–64. https://doi.org/10.1038/s41586-022-05138-6
70. Nguyen T, Li S, Chang JT *et al.* Chromatin sequesters pioneer transcription factor Sox2 from exerting force on DNA. *Nat Commun* 2022;**13**:3988. https://doi.org/10.1038/s41467-022-31738-x
71. Liu K, Grasso EM, Pu S *et al.* Structure and DNA-bridging activity of the essential Rec114-Mei4 trimer interface. *Genes Dev* 2023;**37**:518–34. https://doi.org/10.1101/gad.350461.123
72. Molnar M, Doll E, Yamamoto A *et al.* Linear element formation and their role in meiotic sister chromatid cohesion and chromosome pairing. *J Cell Sci* 2003;**116**:1719–31. https://doi.org/10.1242/jcs.00387
73. Syrjanen JL, Pellegrini L, Davies OR. A molecular model for the role of SYCP3 in meiotic chromosome organisation. *eLife* 2014;**3**:e02963. https://doi.org/10.7554/eLife.02963
74. West AM, Rosenberg SC, Ur SN *et al.* A conserved filamentous assembly underlies the structure of the meiotic chromosome axis. *eLife* 2019;**8**:e40372. https://doi.org/10.7554/eLife.40372
75. Ellermeier C, Smith GR. Cohesins are required for meiotic DNA breakage and recombination in *Schizosaccharomyces pombe*. *Proc Natl Acad Sci USA* 2005;**102**:10952–7. https://doi.org/10.1073/pnas.0504805102
76. Wintrebert M, Nguyen MC, Smith GR. Activation of meiotic recombination by nuclear import of the DNA break hotspot-determining complex in fission yeast. *J Cell Sci* 2021;**134**:jcs253518. https://doi.org/10.1242/jcs.253518
77. Sievers F, Wilm A, Dineen D *et al.* Fast, scalable generation of high-quality protein multiple sequence alignments using Clustal Omega. *Mol Syst Biol* 2011;**7**:539. https://doi.org/10.1038/msb.2011.75

Received: June 8, 2024. **Revised:** January 26, 2025. **Editorial Decision:** February 3, 2025. **Accepted:** February 7, 2025